Tailoring Orbital Angular Momentum of Light in the Visible Domain with Metallic Metasurfaces

Davit Hakobyan, Hernando Magallanes, Gediminas Seniutinas, Saulius Juodkazis, Etienne Brasselet

Tailoring Orbital Angular Momentum of Light in the Visible Domain with Metallic Metasurfaces

*Davit Hakobyan, Hernando Magallanes, Gediminas Seniutinas, Saulius Juodkazis, and Etienne Brasselet**

Submicron-thick gold films endowed with subwavelength patterning allow on-demand topological shaping of light, hence the precise delivery of optical orbital angular momentum. Several kinds of metallic metasurfaces enabling the generation of optical vortices with arbitrary topological charges in the visible domain are fabricated following a design based on space-variant subwavelength grating with discrete orientational distribution. The optical performances of obtained flat spin–orbit optical elements designed to operate at 532 nm wavelength are experimentally assessed and satisfactorily compared to expectations. About 80% of optical vortex generation purity for predetermined topological charge up to $|\ell| = 10$ is achieved. Other designs that allow continuous orientational distribution of nanogratings as well as the superposition of orbital angular momentum states are also proposed.

1. Introduction

Engineering the phase and polarization of light is nowadays routinely achieved in research laboratories, especially in the framework of the so-called singular optics.[1] In particular, several techniques have been developed to generate light beams endowed with phase singularities, commonly named "vortex beams," whose amplitude is proportional to $exp(\imath\ell\varphi)$, with ℓ integer and φ the polar angle in a plane perpendicular to the propagation direction. A major interest in optical vortex beams is the fact that they carry $\pm\ell\hbar$ orbital angular momentum per photon along the beam propagation direction,[2] where ± sign depends on the used complex fields' representation. Initially, the development of devices enabling optical vortex generation has been made at the macroscopic scale by shaping optical wavefronts in various ways. One can mention the use of spiral phase plates,[3,4] computer generated holograms,[5,6] optical mode conversion,[7] lasing on higher-order modes of resonators,[8] light propagation in uniaxial crystals,[9,10] and space-variant birefringent retarders with formed[11] or natural[12] birefringence. Since then, these approaches have been improved and singular photonic technologies have emerged, a large set of products being now available to generate vortex beams. Still, from a practical point of view, mature options remain those relying on bulk and macroscopic optical elements.

Quite naturally, research efforts have been made to miniaturize singular optical devices. For instance, femtosecond 3D direct laser writing technique has been proposed to fabricate microscopic spiral phase plates[13] and easy-prototyping of almost arbitrary singular microoptical elements with standard optical quality is now achievable.[14,15] On the other hand, self-engineered topological defects of liquid crystals have been shown to behave as small-scale optical vortex generators based on spin–orbit interaction of light. In particular, the initial approach based on droplets (1–10 µm diameter)[16] evolved toward the use of thin (10–100 µm thick) films whose efficiency, diversity, tunability, and reconfigurability stand with more than decent figures of merit.[17–20] Another approach consists to functionalize existing integrated optics subsystems with singular features, for instance, by twisting weakly deformed fibers[21] or by using corrugated ring microresonators coupled to waveguides.[22] Of course, above few examples do not aim at providing an exhaustive list of recent progresses and, in order to partly fill this gap, one may refer to ref. [23] for a review of several strategies toward the elaboration of compact singular photonic devices. In particular, the use of ultrathin (i.e., with subwavelength thickness) artificially structured surfaces received a growing interest since a few years, as summarized in several recent reviews.[24–27] The common denominator of these approaches is subwavelength structuring of ultrathin material layer that confers "meta"-properties to it, from which originates the terminology of optical "meta"-surfaces.

In this work, we address the particular case of optical vortex generation with topological charge ℓ up to $|\ell| = 10$, in the visible domain, by using nanostructured metallic thin films following an approach introduced by Hasman's group in the early 2000s in the mid-infrared domain.[11] The idea consists to benefit from the spin–orbit interaction of light owing to azimuthally varying artificially birefringent waveplates made of inhomogeneous subwavelength

D. Hakobyan, H. Magallanes, Dr. E. Brasselet
Univ. Bordeaux
CNRS
Laboratoire Ondes et Matière d'Aquitaine
UMR 5798, F-33400 Talence, France
E-mail: etienne.brasselet@u-bordeaux.fr
D. Hakobyan, G. Seniutinas, Prof. S. Juodkazis
Centre for Micro-Photonics
Swinburne University of Technology
John st., Hawthorn, Vic 3122, Australia

DOI: 10.1002/adom.201500494

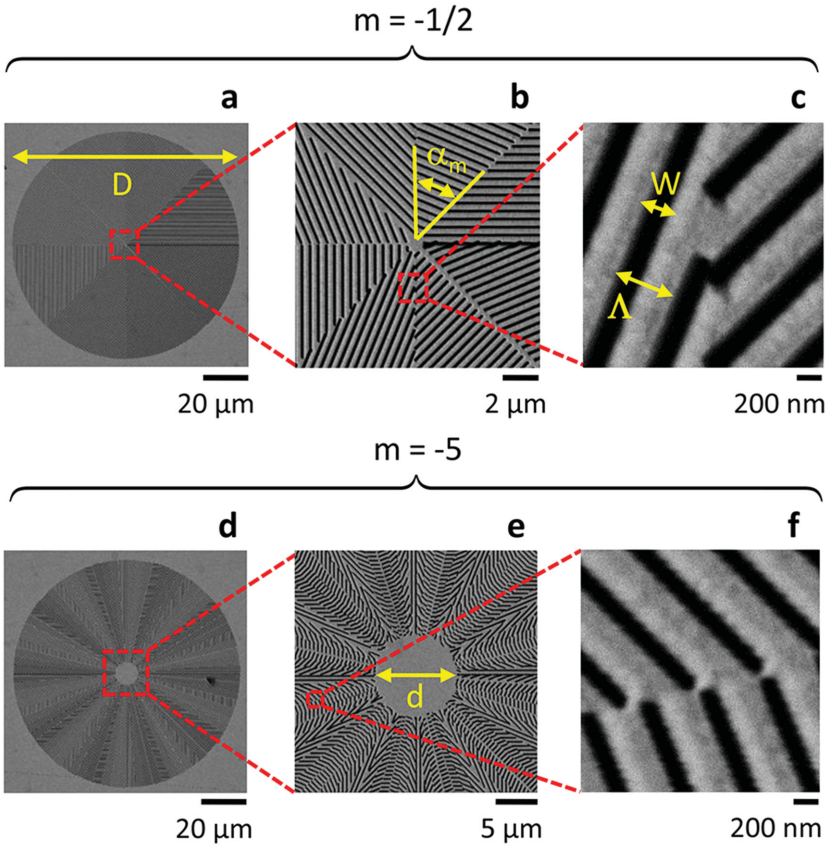

Figure 1. SEM images of a–c) fundamental [$m = -1/2$] and d–f) high-order [$m = -5$] metasurfaces with thickness $h = 300$ µm, diameter $D = 100$ µm, grating period $\Lambda = 500$ nm, and slit width $W = 160$ nm. Each device is made of $16|m|$ sectors of angular width $\alpha_m = \pi/(8|m|)$ with $\pi/8$ steps for the grating orientation between adjacent sectors; see panels (b) and (e). The central part of high-order metasurfaces is purposely left unstructured over a disk of diameter $d = 10$ µm in order to preserve a proper resolution of the azimuthal pattern; see panels (d) and (e).

grating. The process at play can be described in a simplistic—however efficient—manner assuming an incident circularly polarized plane wave $\mathbf{E}_{\text{in}} \propto \mathbf{c}_{\sigma=\pm1}$, where $\mathbf{c}_\sigma = (\mathbf{x} + \imath\sigma\mathbf{y})/\sqrt{2}$ denotes circular polarization unit vector, impinging at normal incidence onto a inhomogeneous and optically anisotropic slab having an azimuthal distribution of the optical axis orientation $\psi(\varphi) = m\varphi$ (m is a half-integer) and a complex birefringent phase retardation $\tilde{\Delta} = \Delta + i\Delta'$. Indeed, neglecting the correcting propagation effects that enrich the radial structure of the output beam,[28] the output light field is expressed as[29]

$$\mathbf{E}_{\text{out}} \propto \cos(\tilde{\Delta}/2)\,\mathbf{c}_\sigma + i\sin(\tilde{\Delta}/2)e^{i2\sigma m\varphi}\,\mathbf{c}_{-\sigma} \tag{1}$$

Above equation emphasizes that the polarization conversion process $\mathbf{c}_\sigma \to \mathbf{c}_{-\sigma}$ is associated with the generation of an on-axis optical phase singularity with topological charge $\ell = 2\sigma m$. That is to say, the $\mathbf{c}_{-\sigma}$-polarized component of the output light field carries an orbital angular momentum $\ell\hbar$ per photon. The figure of merit of such a spin–orbit interaction process is then evaluated by the quantity $\eta = (|\mathbf{E}_{\text{out}} \cdot \mathbf{c}_\sigma|^2)/|\mathbf{E}_{\text{out}}|^2 = |\sin(\tilde{\Delta}/2)|^2$, called purity in what follows, that is expressed as

$$\eta = \frac{(1-\delta)^2\cos^2(\Delta/2) + (1+\delta)^2\sin^2(\Delta/2)}{2(1+\delta^2)} \tag{2}$$

where $\delta = e^{-\Delta'}$ refers to the dichroic character of the metasurface.

Experimentally, an ideal design should satisfy a maximum purity $\eta = 1$. From Equation (2) this corresponds to the double condition $\Delta = (2n+1)\pi$ (n is an integer) and $\delta = 1$. For this purpose, we used a design inferred from previous numerical simulations performed for gold nanogratings,[30] which is described in Section 2, where the structural characterization of the fabricated micro-optical elements is also presented. Then, we report in Section 3 on the generation of optical vortex beams with predetermined topological charges and quantify the performances of our metasurfaces. Finally, our results are discussed in the framework of previous metallic nanostructure approaches that aim at tailoring the optical orbital angular momentum of the visible light. Transmission issue is also addressed; indeed optimal devices are obtained when maximum purity meets maximum transmission.

2. Metallic Metasurfaces: Design, Fabrication, and Characterization

Following numerical analysis reported in ref. [30], we designed optimal gold metasurfaces with diameter D = 100 µm for 532 nm wavelength. By choosing layer thickness h = 300 nm, grating period Λ = 500 nm, and slit width W = 160 nm, one actually expects $\Delta \simeq \pi$ and $\delta \simeq 1$.[30] In practice, we opted in favor of a piecewise pattern made of $16|m|$ sectors with identical angular width $_m = \pi/(8|m|)$ and $\pi/8$ orientational steps between two adjacent sectors. Metallic metasurfaces are patterned via direct ion beam lithography, and scanning electron microscope (SEM) images of structures with $m = -1/2$ and $m = -5$ are shown in **Figure 1**.

The fabrication protocol is identical for all realized structures. It starts with a 500 µm thick BK7 glass used as a substrate for metal deposition. The substrate is sonicated for 10 min in acetone and methanol to remove contamination and enhance surface adhesion for metal deposition. Then, a 5 nm adhesion layer of chromium is electron beam evaporated, followed by a magnetron sputtered 300 nm thick gold layer using the same deposition system (K. J. Lesker, AXXIS) without breaking the vacuum. The coated substrates are then placed into a lithography system (Raith, IonLiNE) where focused Ga^+ ions are used to mill the designed patterns. The central part of high-order metasurfaces is purposely left unstructured over a disk of diameter $d = 10$ µm in order to preserve a proper resolution of the azimuthal pattern, which corresponds to a negligible fraction (1%) of the whole metasurface area.

The inhomogeneous optical properties of the fabricated metasurfaces are retrieved by determining the spatial distribution of the output polarization ellipse azimuth angle, $\Phi(x,y)$,

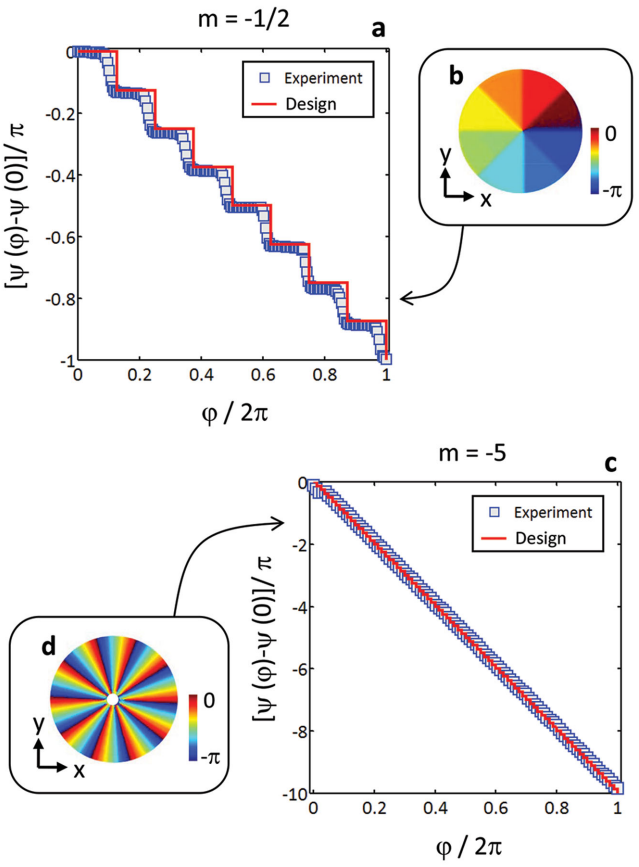

Figure 2. Optical characterization of the space-variant optically anisotropic features of metasurfaces of order $m = -1/2$ and $m = -5$. a,c) Local optical axis orientation angle ψ as a function of the azimuthal angle φ. b,d) Insets refer to experimental 2D maps of the angle ψ in the (x,y) plane.

under circularly polarized illumination. Indeed, neglecting dichroism, Φ lies at a $\pm 45^{\circ}$ angle from the local optical axis angle ψ depending on the actual values of the birefringent phase retardation and the incident polarization handedness. In practice, ψ is therefore determined by recording a set of four images of the structure illuminated by circularly polarized light with almost uniform intensity distribution over the metasurface by placing at the output of the structure a polarizer at four different angles separated by 45°; see ref. [16] for details. The results are shown in **Figure 2** for the structures presented in Figure 1, noting that one has by construction $\Phi(\varphi) - \Phi(0) = \psi(\varphi) - \psi(0)$. The measured spatial distribution of the optical axis orientation follows the pattern expected from the design; see the red curves in Figure 2.

3. Topological Shaping of Light: Generation of Optical Vortex Beams

The generation of vortex beams as such is explored by illuminating the metasurface at normal incidence with a $\mathbf{c}_{\sigma}$ circularly polarized paraxial Gaussian laser beam at 532 nm wavelength. The sample is located at the focal plane of the Gaussian beam, where the beam waist radius at exp(−2) from its maximal intensity is $w_0 \simeq 25\,\mu\text{m}$. We can thus consider that all incident light is processed by the metasurface and, since the associated beam divergence is $\theta_0 \simeq 0.4$, the plane-wave formulation of the spin–orbit interaction process described by Equation (1) can be fairly used in practice.

Since the optical vortex is embedded in the $\mathbf{c}_{-\sigma}$-polarized component of the output light beam, it can be selected by placing after the sample a quarter-waveplate followed by a linear polarizer oriented at a $-\sigma 45^{\circ}$ angle from the quarter-waveplate slow axis. The intensity profiles of the vortex beams obtained from metasurfaces with order $m = 1/2$ and $m = 5$ are shown in **Figure 3**a,d. As expected, a doughnut pattern with zero on-axis intensity is obtained for $m = 1/2$, whereas for $m = 5$ a spurious on-axis hot spot is observed in the center of the doughnut intensity profile, which results from the unstructured central part (see Figure 1d,e).

On the other hand, the spiraling spatial distribution of the phase of the generated vortex beam is experimentally assessed by scrutinizing the interference pattern obtained from its coherent superposition with a reference Gaussian beam having identical polarization state. The resulting $2|m|$-arm spiraling intensity patterns, whose handedness depends on the helicity σ of the incident light, are shown in Figure 3b,c for $m = 1/2$ and in Figure 3e,f for $m = 5$. These results clearly indicate the generation of on-axis optical phase singularity with topological charge $\ell = 2\sigma m$, as expected from Equation (1).

The performance of the metasurfaces regarding their ability to tailor the orbital angular momentum of light is then evaluated by measuring the power $P_{\pm\sigma}$ of the $\mathbf{c}_{\pm\sigma}$-polarized component of the output light beam, which are respectively selected by orienting the linear polarizer at a $\pm\sigma 45^{\circ}$ angle from the quarter-waveplate slow axis. From the definition of the purity η, one thus gets $\eta = P_{-\sigma}/(P_{\sigma} + P_{-\sigma})$. We find $\eta \simeq 78\%$ independently of the metasurface order m. Obviously, the actual figure of merit of the metasurfaces does not meet the expectation from the optimal design that implies $\eta = 100\%$, which can be attributed to unavoidable fabrication imperfections.

Still, it is worth considering which of the real or imaginary parts of the complex birefringent retardation $\tilde{\Delta}$ is the most detrimental to reach optimal performances. For this purpose, we fabricated a $100\,\mu\text{m} \times 100\,\mu\text{m}$ straight grating (i.e., $m = 0$) with identical thickness, period, and slit width as before. Indeed, δ can be estimated from the ratio between the power $P_{\parallel,\perp}$ of the output light beam when the incident beam is linearly polarized along and perpendicular to the grating wavevector. Namely, $\delta = (P_{\parallel}/P_{\perp})^{1/2}$ and we find $\delta \simeq 0.95$. Combining this value to the measurement of η, Equation (2) allows us to deduce $\Delta \simeq 0.7\pi$ or 1.3π. The fact that positions of metasurface slit segments were slightly shifted with respect to one another due to sample thermal drifting over a long fabrication time (a few hours for one device) is likely to be part of the explanation for the observed 30% deviation from the designed value for Δ.

We also explored the broadband performances of the metasurfaces by demonstrating white light vortex generation. This is done by using a halogen lamp as a polychromatic source and achromatic quarter-waveplates to prepare and select input/output contracircular polarization states over the visible domain. In practice, we prepared a secondary white light source

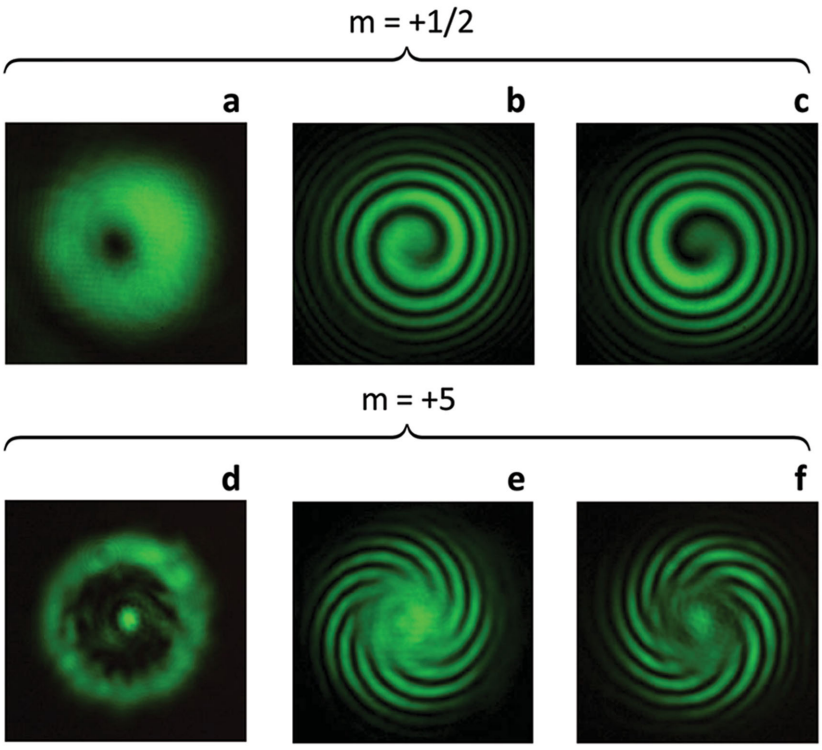

Figure 3. Experimental intensity pattern of the circularly polarized component of the output vortex field whose polarization state is orthogonal to the incident circularly polarized Gaussian beam in the case of a) $m = 1/2$ and d) $m = 5$. Interference pattern of the generated optical vortex beam of charge $\ell = 2\sigma m$ with a coaxial Gaussian beam for two different incident helicities $\sigma = \pm 1$; see panels b) and c) for $m = 1/2$ and panels e) and f) for $m = 5$.

by using a 100 µm diameter pinhole that allows us to increase the spatial coherence of the polychromatic source. This allows clear visual identification of the characteristic doughnut intensity profile of a white light vortex beam; see **Figure 4**a in the case of $m = 1/2$, where its red, green, and blue spectral components (bandpass filters with 3 nm full-width half-maximum (FWHM) transmission spectrum) are also shown. The yellowish color of the white light vortex intensity pattern shown in Figure 4a is reminiscent of the dispersive characteristics of the metallic nanostructure, which suggests a wavelength-dependent optical vortex generation process. Experimentally, this is explored by measuring the purity η in the visible domain by using a set of nine bandpass filters whose central wavelengths are separated by 50 nm and with 10 nm FWHM transmission spectrum. An additional measurement is performed by using a bandpass filter for 532 nm wavelength with 3 nm FWHM transmission spectrum, which gives a bit lower purity (≃70%) than the one measured with 532 nm laser radiation. The results for $m = 1/2$ are shown in Figure 4b that emphasize the broadband capabilities of the metallic nanostructures.

4. Discussion

Quite surprisingly, the quantitative comparison of the present experimental results to the previous metallic approaches in the visible domain is not an easy task due to the lack of precise information found in the literature. This refers to ref. [30] whose numerical developments have been used here to design our structures and where the experimental generation of radially polarized beams at 633 nm wavelength from discrete space-variant subwavelength gratings is reported. Besides the use of inhomogeneous gratings, there are several studies based on the use of plasmonic nanoantennas of various shapes to address topological shaping of light.[24–27] In particular, there is a recent work dealing with L-shaped nanoantennas that provides with a detailed performance analysis,[31] though in the near infrared range 760 – 790 nm. In that work, an experimental purity $\eta \simeq 10\%$ is achieved[31] whereas an improvement up to $\eta \simeq 35\%$ has been very recently reported[32] (note that "purity" ρ introduced in ref. [32] is related to our definition of η via the relationship $\eta = \rho/(1+\rho)$). That is to say, our experimental attempt to generate light beams with well-defined orbital angular momentum states in the visible domain appears to be fairly good. From a theoretical point of view, we note a very recent study on optical vortex generation using corrugated metallic nanowires at 1.5 µm wavelength.[33] The latter work, which accounts metal losses, reports on efficiencies of 35% for $\ell = 1$ and 60% for $\ell = 2$, which correspond to purity of 90% and 97%, respectively, recalling that efficiency equals purity times transmission.

An alternative option to generate optical vortex beams from space-variant subwavelength grating is to consider continuous rather than discrete orientational distribution. In fact, it has been proposed that closed-path nanoslits endowed with geometrical cusps allow the effective optical axis orientation angle ψ to cover any integer multiple of the range $0 \le \psi \le \pi$.[34] Typical examples are found looking at the family of curves that correspond to the trajectory of a point attached to a given circle as it rolls without slipping within and around another fixed circle, namely hypocycloids (subscript h) and epicycloids (subscript e). These classes of curves are basically described by their number of cusps $m_h \ge 3$ and $m_e \ge 1$, and characterized by a circulation along their contour $s = \frac{1}{2\pi}\oint d\psi$, which is equal to $s_h = 1 - m_h/2$ and $s_e = 1 + m_e/2$. The light field just after sample is thus characterized by the topological charge $\ell = 2\sigma s$ for the contracircularly output component generated by spin–orbit interaction in the case of circularly polarized incident light.[34] The hypocycloid-like case (i.e., constructed from arcs of circles) has been investigated experimentally in ref. [35] and here we report on the actual hypo/epicycloids; see **Figure 5**a–f where the characterization of inhomogeneous birefringent properties is shown for a set of structures with increasing number of cusps. The latter data confirm continuous mapping for ψ with $s_h = (-1/2, -1, -3/2)$ (Figure 5a–c) and $s_e = (3/2, 2, 5/2)$ (Figure 5d–f). On the other hand, the effective birefringent phase retardation evaluated at 546 nm wavelength is found to be $\Delta \simeq 0.07\pi$ for $h = 60$ nm

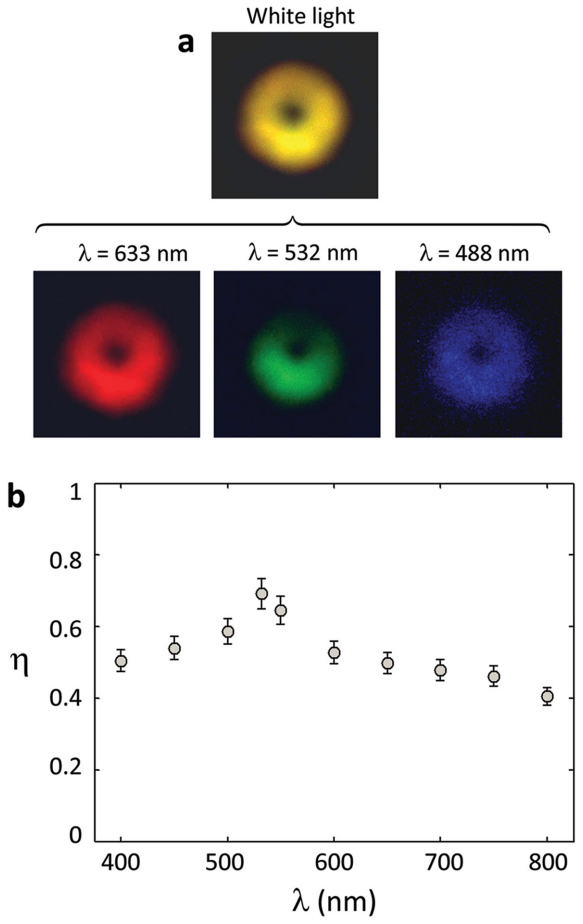

Figure 4. Polychromatic optical vortex generation for the structure of order $m = 1/2$ using a halogen lamp. a) Intensity pattern of the generated polychromatic optical vortex is shown with its red, green, and blue spectral components. b) Wavelength dependence of the purity η in the visible domain.

and $W = 400$ nm, $\Delta \simeq 0.2\pi$ for $h = 60$ nm and $W = 70$ nm, and $\Delta \simeq 0.55\pi$ for $h = 200$ nm and $W = 40$ nm, which correspond to the explored set of parameters.

Although the cusped approach is attractive as such, practical limitations arise from small geometrical cross-section of a single slit. This issue can be addressed by considering nested geometries; see Figure 5 where SEM (panels (g) and (h)) and polarimetric birefringent imaging (panels (i) and (j)) of five nested hypocycloidal slits with $m_h = 3$ and $m_h = 4$ are shown. Noting that fabrication capabilities allow us to realize any combination of slit geometries, one may consider to generate arbitrary superposition of vortex beams from a single circularly polarized light beam with possible use for creation and manipulation of 3D knotted and linked lines of zero intensity embedded in a beam.[36] As an example of multifunctional element, **Figure 6** shows optical profilometer images of 60 nm thick, 20 μm diameter gold disks endowed with 150 nm width hypocycloidal slits of orders $m_h = 3$ (panel (a)), $m_h = 4$ (panel (b)), and $m_h = 5$ (panel (c)), which combine at the micron scale both negative (hypocycloid geometry) and positive (circle geometry[37]) circulations of the optical axis angle ψ. This particular example allows us to emphasize that edges also allow spin–orbit interaction, though in a less efficient manner than slits; indeed, polarimetric birefringent imaging measurements give effective birefringent phase retardations evaluated at 546 nm wavelength $\Delta_{edge} \simeq 0.03\pi$ and $\Delta_{slit} \simeq 0.07\pi$ for the structures shown in Figure 6.

Noteworthy, the relatively low power transmission of the studied micro-optical elements nevertheless appears as a serious practical issue. Indeed, although efficient, the topological shaping of light obtained with present structures corresponds to an $\simeq 2\%$ power transmission. To address this issue, the use of dielectric metasurfaces should be considered, which is a recent topic[38] that has already led to many interesting developments in beam shaping in the near-infrared domain ($\lambda \approx 1.5$ μm) where silicon offers high transmission.[39–42] Still,

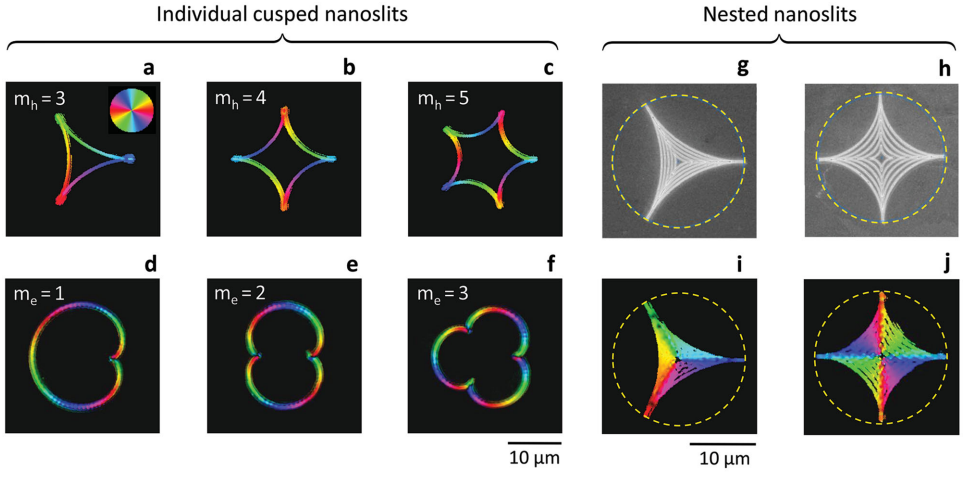

Figure 5. Experimental reorientation map reconstructed from polarimetric birefringent imaging of cusped closed-path nanoslits inscribed in a 20 μm diameter circle in the case of a–c) 200 nm thick, 40 nm width hypocycloidal slits with $m_h = (3,4,5)$ and d–f) 60 nm thick, 400 nm width epicycloidal slits with $m_e = (1,2,3)$. Luminance is proportional to the effective birefringent phase retardation Δ whereas the colormap refers to the orientation angle of the local optical axis ψ as shown up-right in panel (a). g,h) SEM picture of five nested 60 nm thick, 70 nm width hypocycloidal slits for $m_h = 3$ and $m_h = 4$, where the dashed circle has 20 μm diameter. i,j) Corresponding polarimetric birefringent imaging.

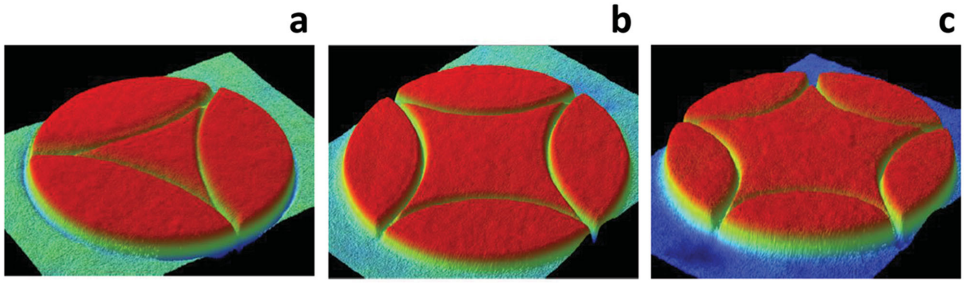

Figure 6. a–c) Optical profilometer images of multifunctional nanostructured micro-optical elements made of 60 nm thick, 20 μm diameter gold disks endowed with 150 nm width hypocycloidal slits of order m_h = 3, 4 and 5, respectively.

the dielectric analog of present metallic structures would also suffer from dispersion regarding the broadband optical vortex generation capabilities. Although the quantitative analysis of such an issue is beyond the scope of the present study, one can suppose that appropriate choice of materials and substructure design of the nanograting grooves could lead to interesting broadband properties. Nevertheless, the metallic approach remains endowed with valuable added values such as plasmonic resonances, and it is likely that hybrid metasurfaces combining metallic and dielectric features will offer new functionalities.

5. Summary

We reported on the fabrication and characterization of small-scale optical vortex generators made of metallic metasurfaces following the known concept of space-variant subwavelength gratings that relies on spin–orbit interaction of light. The realized nanostructured micro-optical elements allow efficient tailoring of the orbital angular momentum of light in the visible domain. Topological shaping of light with purity up to ≃80 % has been achieved and the broadband performances of the metasurfaces have been investigated. Also, we discussed discrete versus continuous approach regarding the spatial distribution of effective optical axis arising from subwavelength structuring as well as the possible realization multifunctional topological optical elements.

Acknowledgements

D.H. and E.B. thank financial support from the French State in the frame of the Investments for the future Programme IdEx Bordeaux (reference ANR-10-IDEX-03-02) and COST Action MP1205. H.M. thanks financial support from CONACYT Mexico. S.J. and G.S. are grateful for a partial support via the Australian Research Council project DP130101205. The authors are grateful to G. Gervinskas for an early contribution to this study.

Received: September 5, 2015
Revised: September 29, 2015
Published online: November 16, 2015

[1] M. S. Soskin, M. V. Vasnetsov, *Prog. Opt.* **2001**, *42*, 219.
[2] L. Allen, M. W. Beijersbergen, R. J. C. Spreeuw, J. P. Woerdman, *Phys. Rev. A* **1992**, *45*, 8185.
[3] S. N. Khonina, V. V. Kotlyar, M. V. Shinkaryev, V. A. Soifer, G. V. Uspleniev, *J. Mod. Opt.* **1992**, *39*, 1147.
[4] M. Beijersbergen, R. Coerwinkel, M. Kristensen, J. Woerdman, *Opt. Commun.* **1994**, *112*, 321.
[5] N. R. Heckenberg, R. McDuff, C. P. Smith, A. G. White, *Opt. Lett.* **1992**, *17*, 221.
[6] I. Basistiy, V. Bazhenov, M. Soskin, M. Vasnetsov, *Opt. Commun.* **1993**, *103*, 422.
[7] M. W. Beijersbergen, L. Allen, H. E. L. O. van der Veen, J. P. Woerdman, *Opt. Commun.* **1993**, *96*, 123.
[8] M. Harris, C. A. Hill, P. R. Tapster, J. M. Vaughan, *Phys. Rev. A* **1994**, *49*, 3119.
[9] A. Volyar, T. Fadeyeva, *Opt. Spectrosc.* **2003**, *94*, 235.
[10] A. Ciattoni, G. Cincotti, C. Palma, *J. Opt. Soc. Am. A: Opt. Image Sci. Vis.* **2003**, *20*, 163.
[11] G. Biener, A. Niv, V. Kleiner, E. Hasman, *Opt. Lett.* **2002**, *27*, 1875.
[12] L. Marrucci, C. Manzo, D. Paparo, *Phys. Rev. Lett.* **2006**, *96*, 163905.
[13] G. Knöner, S. Parkin, T. A. Nieminen, V. L. Y. Loke, N. R. Heckenberg, H. Rubinsztein-Dunlop, *Opt. Express* **2007**, *15*, 5521.
[14] E. Brasselet, M. Malinauskas, A. Žukauskas, S. Juodkazis, *Appl. Phys. Lett.* **2010**, *97*, 211108.
[15] A. Žukauskas, M. Malinauskas, E. Brasselet, *Appl. Phys. Lett.* **2013**, *103*, 181122.
[16] E. Brasselet, N. Murazawa, H. Misawa, S. Juodkazis, *Phys. Rev. Lett.* **2009**, *103*, 103903.
[17] E. Brasselet, C. Loussert, *Opt. Lett.* **2011**, *36*, 719.
[18] R. Barboza, U. Bortolozzo, G. Assanto, E. Vidal-Henriquez, M. G. Clerc, S. Residori, *Phys. Rev. Lett.* **2012**, *109*, 143901.
[19] E. Brasselet, *Phys. Rev. Lett.* **2012**, *108*, 087801.
[20] C. Loussert, U. Delabre, E. Brasselet, *Phys. Rev. Lett.* **2013**, *111*, 037802.
[21] C. N. Alexeyev, A. N. Alexeyev, B. P. Lapin, G. Milione, M. A. Yavorsky, *Phys. Rev. A* **2013**, *88*, 063814.
[22] X. Cai, J. Wang, M. J. Strain, B. Johnson-Morris, J. Zhu, M. Sorel, J. L. O'Brien, M. G. Thompson, S. Yu, *Science* **2012**, *338*, 363.
[23] M. Q. Mehmood, C.-W. Qiu, A. Danner, J. Teng, *J. Mol. Eng. Mater.* **2014**, *2*, 144013.
[24] N. Yu, F. Capasso, *Nat. Mater.* **2014**, *13*, 139.
[25] Y. Zhao, X.-X. Liu, A. Alu, *J. Opt.* **2014**, *16*, 123001.
[26] P. Genevet, F. Capasso, *Rep. Prog. Phys.* **2015**, *78*, 024401.
[27] G. Rui, Q. Zhan, *Nanophotonics* **2015**, *4*, 2.
[28] E. Karimi, B. Piccirillo, L. Marrucci, E. Santamato, *Opt. Lett.* **2009**, *34*, 1225.
[29] E. Brasselet, *Opt. Lett.* **2013**, *38*, 3890.
[30] K. Iwami, M. Ishii, Y. Kuramochi, K. Ida, N. Umeda, *Appl. Phys. Lett.* **2012**, *101*, 161119.
[31] F. Bouchard, I. D. Leon, S. A. Schulz, J. Upham, E. Karimi, R. W. Boyd, *Appl. Phys. Lett.* **2014**, *105*, 101905.
[32] S. A. Schulz, J. Upham, F. Bouchard, I. D. Leon, E. Karimi, R. W. Boyd, in Proc. 6th Int. Conf. Metamaterials, Photonic Crystals and Plasmonics, August 4–7, 2015, New York, USA **2015**, p. 721 .

[33] C. Huang, X. Chen, A. Oladipo, N. Panoiu, F. Ye, *Sci. Rep.* **2015**, *5*, 13089.
[34] E. Brasselet, *Opt. Lett.* **2013**, *38*, 2575.
[35] E. Brasselet, G. Gervinskas, G. Seniutinas, S. Juodkazis, *Phys. Rev. Lett.* **2013**, *111*, 193901.
[36] M. R. Dennis, R. P. King, B. Jack, K. O'Holleran, M. J. Padgett, *Nat. Phys.* **2010**, *6*, 118.
[37] P. F. Chimento, P. F. A. Alkemade, G. W. 't Hooft, E. R. Eliel, *Opt. Lett.* **2012**, *37*, 4946.
[38] D. Lin, P. Fan, E. Hasman, M. L. Brongersma, *Science* **2014**, *345*, 298.
[39] M. Decker, I. Staude, M. Falkner, J. Dominguez, D. N. Neshev, I. Brener, T. Pertsch, Y. S. Kivshar, *Adv. Opt. Mater.* **2015**, *3*, 813.
[40] M. I. Shalaev, J. Sun, A. Tsukernik, A. Pandey, K. Nikolskiy, N. M. Litchinitser, *Nano Lett.* **2015**, *15*, 6261.
[41] B. Desiatov, N. Mazurski, Y. Fainman, U. Levy, *Opt. Express* **2015**, *23*, 22611.
[42] K. E. Chong, I. Staude, A. James, J. Dominguez, S. Liu, S. Campione, G. S. Subramania, T. S. Luk, M. Decker, D. N. Neshev, I. Brener, Y. S. Kivshar, *Nano Lett.* **2015**, *15*, 5369.